https://doi.org/10.1016/j.polymer.2022.125195

Effects of electron irradiation on structure and bonding of polymer spherulite thin films

Changsheng Chen‡, Xuyun Guo‡, Guangming Zhao, Yunduo Yao, Ye Zhu*

Department of Applied Physics, Research Institute for Smart Energy, The Hong Kong Polytechnic University, Kowloon, Hong Kong, China

* Corresponding Author. Email address: yezhu@polyu.edu.hk; ORCID: 0000-0002-5217-493X.

‡ These authors contributed equally.

ABSTRACT

We report the detailed beam effects in PE, PCL, and P3HT spherulite thin films, including both structure and chemical bonding evolution detected from quantitative electron diffraction and spectroscopy. Both amorphization and mass loss from electron beam irradiation have been clearly identified, most of which can be suppressed effectively by cryo-protection. The initial dominant beam effect in PE and PCL thin films is the radiolysis of C-H bonds, leading to both amorphization and the formation of unsaturated polyenyl groups that further cause lattice expansion. When the samples become mostly amorphous, the mass loss effect becomes prevailing. On the other hand, P3HT exhibits an intriguing two-stage damage process with the side-chain ordering destroyed prior to the π-stacking ordering. Our results not only shed light on the detailed beam effects on structure and chemical bonding in the three polymers, but also demonstrate a powerful approach to quantitatively analyze these effects in other organic solids.

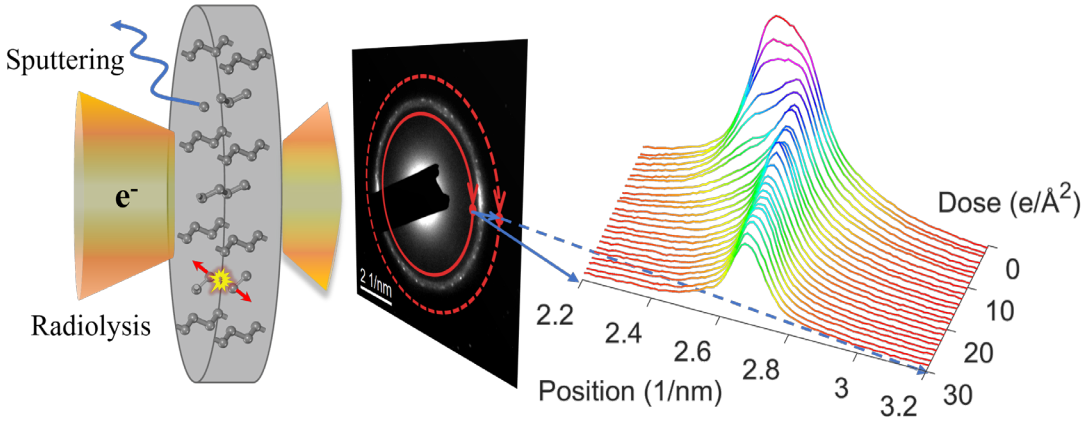

Graphical abstract

Keywords: Polymer; spherulite thin films; electron beam effects; TEM; EELS.

INTRODUCTION

Owing to the unmatched spatial resolution and remarkable versatility, transmission electron microscopy (TEM) has become an indispensable tool to investigate the local material structure and chemistry at the nanometer and atomic scale. However, the power of TEM comes with a limit: the fundamental electron-matter interaction, which underlies the extraordinary characterization capability of TEM, can be too strong for light, soft and weakly-bonded materials. As a result, atoms in crystal lattice can be displaced to interstitial positions or even sputtered out from surface directly by the incident electron beam, the so-called knock-on damage; and energy transferred from the electron beam through inelastic scattering can heat the sample or break the bonding to cause decomposition, the heating and radiolysis effect [1-7]. Materials can be modified or even destroyed by these beam effects before their intrinsic structural information is achieved [8-11]. It is thus vitally important to comprehend the electron beam effects on such beam-sensitive materials, in order to probe their intrinsic structure with minimal artifacts.

As a typical class of beam-sensitive materials, organic solids exhibit a variety of functionalities underpinned by their structure and chemical bonding [12]. For example, properties of semi-crystalline polymers are largely determined by their level of crystallization [13]. Performance of organic semiconductor devices such as organic photovoltaics and light-emitting devices also relies sensitively on their complex nanostructures and morphologies, which needs to be examined by TEM under the risk of beam damage. A variety of local structural information including crystallinity [14], crystalline orientation [15] and structure [9,16-18], band structure [19-21], and radical groups [22,23] can be achieved from organic solids by TEM-based techniques such as

electron diffraction and electron energy loss spectroscopy (EELS). Despite the tremendous potential of TEM characterization on organic materials, however, the electron beam effects that can modify the structure and morphology must be well understood. Beam effects have been studied widely on various organic solids by monitoring the fading of electron diffraction signals and the change of diffraction peak positions [24-26]. EELS has also been used to probe the bonding change caused by beam effects [10,27-30]. More recently, Leijten et al. have developed an approach to reveal polymer film deformation and mass loss using TEM imaging [24]. Based on these techniques, it has been reported that beam effects generally rise with increasing electron dose on organic solids, which may also depend on dose rate, electron energy, temperature, and sample preparation methods [1,7,10,24,25,31]. Lowering sample temperature and increasing accelerating voltage can suppress beam effects in most polymers [1,7,25,32], and recently the ultrafast (down to femtosecond) pulsed-beam approach also offers a new prospect [29,33,34]. Oxygen- and water-free sample preparation and addition of antioxidants can also mitigate beam damage effectively [10,11,24]. On the other hand, with few exceptions [10,24], most of the above works only rely on one technique and do not distinguish different types of beam effects that may occur simultaneously. Moreover, in semicrystalline polymers such as spherulites, amorphous and crystalline phases coexist and may exhibit distinct behavior upon electron beam irradiation, which demands further investigation to distinguish the beam effects in both phases.

Herein, we study the effects of electron exposure on three widely-used polymers, polyethylene (PE), poly(ε-caprolactone) (PCL) and Poly(3-hexylthiophene) (P3HT), in the form of semicrystalline spherulite thin films. We adopt selected-area electron diffraction

(SAED), an established low-dose technique with excellent sensitivity to structure variations, and quantitative curve modeling to reveal the structure and phase evolution under the calibrated electron dose. Both crystalline and amorphous components are analyzed to derive different types of beam effects, in contrast to most of the previous studies that consider the crystalline components only and ignore the amorphous part [25], or just take them as a whole [10,11,24]. EELS is further used to probe the change of chemical bonding, which helps to illustrate the underlying damage mechanism. Measurements are carried out at both room temperature (RT) and cryogenic temperature (~98K), a comparison between which clearly demonstrates the effectiveness of cryo-protection on preventing the beam effects.

MATERIALS AND METHODS

Materials and TEM Sample Preparation. PE (Mw ~ 110 kg/mol, 20 mg, density ~ 0.95 g/cm^2, from Alfa Aesar) was initially dissolved in 1 ml decalin (from Sigma-Aldrich) at 180 ℃ for 3 h to ensure complete dissolution. Then PE films were spin-coated on silicon wafers with 300 nm SiO_2 on the surface, at 4000 rpm for 60 s. All the items used in spin coating including the solution, wafer substrates, glass droppers and the spin-coating disks were pre-heated at 180 ℃ for at least 5 min to prevent uncontrollable rapid crystallization. PCL (80 mg, Mw ~ 14 kg/mol, Mn ~ 10 kg/mol, from Sigma-Aldrich) was dissolved in 1 ml m-xylene (from TCI) at RT for 1 h and subsequently spin-coated on wafers at 4000 rpm for 30 s. P3HT (6 mg, Mw ~ 58 kg/mol, regioregularity > 90%, from Rieke Metals Inc.) was dissolved in 1 ml toluene (from Ourchem) at 80 ℃ for 4 h and then spin-coated on wafer at 4000 rpm for 60 s. In order to increase the crystallinity of P3HT thin film, it was annealed under CS_2 vapor at 40 ℃. All three thin films were transferred onto TEM grids:

thin films with underlying wafers were immersed in hydrofluoric acid aqueous solution to etch the SiO_2 interlayers away. Thin films floating on solution surface were then picked up by TEM grids (**Fig.** S1 in Supplementary Information). The film thicknesses of PE, PCL and P3HT were about 150 nm, 200 nm, and 15 nm, respectively, measured by the profilometer (DEKTAX TX, BRUKER). Maltese crosses are observed from all films using polarized light microscopy (see **Fig.** S2 in Supplementary Information), confirming their spherulite structure.

TEM Operation. TEM observation was performed on a JEOL JEM-2100F microscope operated at 200 kV. In TEM mode, the electron beam (beam current ~2.2 nA) was fully spread to a diameter ~12 μm to achieve a low-dose condition with the dose rate ~1.2 e/(Å^2·s) calculated by the expression below (1):

$$Dose\ rate\ \left[e/(\text{Å}^2 \cdot s\ )\right] = \frac{I_{probe}\cdot 10^{-9}\ [6.24\cdot 10^{18}\ [e/s]]}{Area_{illuminating}} \quad (1)$$

The SAED patterns were taken with a selected-area aperture ~4.2 μm in diameter on a Gatan Orius SC 1000A camera, with exposure time 0.3 s and acquisition intervals 0.7 s for PE and P3HT, and 0.3-1.2 s for PCL, respectively. The samples were under continuous illumination without beam blocking during observation. The electron dose for each SAED pattern was derived based on the total illumination time before the pattern recording plus half of the acquisition time (representing the average dose during pattern recording). For cryogenic observation, the polymer samples were loaded into a liquid-nitrogen cooling holder (Gatan, model 636) to lower temperature down to 98 K. The system was stabilized for over 40 min after filling the liquid nitrogen, in order to minimize vibration caused by liquid nitrogen evaporation. EELS was carried out using a Gatan Enfina spectrometer with the energy dispersion 0.05 eV per channel in scanning TEM (STEM) mode, with the 13

mrad convergence angle and 21 mrad collection angle. The STEM forms a 0.5 nm probe with the beam current ~28.5 pA. EEL spectra were taken with the probe scanning typically over ~94×94 nm^2 area with pixel size ~0.37 nm/pixel and dwell time ~2.5 s/pixel, thus a dose rate ~200.5 e/($Å^2$·s). The dose for STEM-EELS was calculated by multiplying the dose rate with the total illumination time before the acquisition plus half of the acquisition time. For low-loss EELS, the reflected tail approach was used to remove the tail of the zero-loss peak.

RESULTS AND DISCUSSION

Typical SAED patterns taken from a PE film at ~98 K are presented in **Fig.** 1a. The pristine film (0.6 e/$Å^2$ dose for acquiring the first SAED pattern) shows polycrystalline PE structure with sharp arcs corresponding to 110, 200 and 020 diffraction. The appearance of diffraction arcs instead of complete rings is attributed to the range of the selected area (~4.2 μm), which is only part of the spherulite thin films and thus does not show a complete circular symmetry. The vulnerability of PE films under the high-energy electron beam is evidenced in the after-exposure image on the right: after accumulating only 8 e/$Å^2$ dose, the 110 diffraction ring becomes dimmer and diffuse, while the 200 and 020 diffraction becomes nearly invisible, indicating the diminished lattice ordering upon beam exposure. Furthermore, all diffraction rings show reduced radii compared to the pristine diffraction pattern, suggesting enlarged lattice spacing caused by the electron beam. To analyze these structure evolutions quantitatively, we perform radial averaging on SAED patterns to obtain the diffraction intensity curves (**Fig.** 1b and 1c) and model the curves using least-squares fitting [24]. As illustrated in **Fig.** 1b, by subtracting the radial-averaged intensity profile by a power-law background [24] and a constant for residual dark counts, the

remaining diffraction signals can be adequately fitted with three Gaussians ($R^2 \geq 99.5\%$): two for 110 and 200 diffraction and one for the signal from the amorphous phase. Thus, the total diffraction intensity can be described by the equation.

$$I = a_1 e^{-\frac{(x-b_1)^2}{2c_1^2}} + a_2 e^{-\frac{(x-b_2)^2}{2c_2^2}} + a_3 e^{-\frac{(x-b_3)^2}{2c_3^2}} + dx^{-\gamma} + e \qquad (2)$$

Besides the peak position indicated by b_i, intensity of each diffraction peak can also be derived from the area of the fitted Gaussian, which reflects the corresponding ordering (or disordering for the amorphous peak). As 110 and 200 are the dominating diffraction peaks, we take the sum of two peak intensity I_{110} and I_{200} as the total crystal diffraction intensity I_{cryst} without considering other minor diffraction such as 020. Then the sum of I_{cryst} and $I_{amorphous}$ is just the total background-subtracted intensity in equation (2). We note that the fitted amorphous peak position matches closely with the reported value from x-ray diffraction on amorphous PE [N1 35], validating the reliability of our quantitative fitting process.

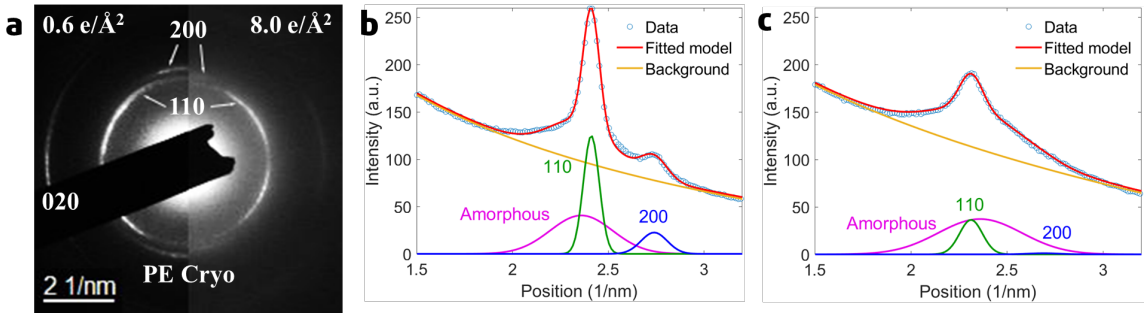

Fig. 1. (a) SAED patterns on the same PE film at 98 K (cryo) with the dose 0.6 (left) and 8.0 (right) e/Å^2, respectively. (b, c) Intensity profiles from radial averaging on SAED patterns in (a), with the dose (b) 0.6 and (c) 8.0 e/Å^2, respectively. Gaussian fitting is used to measure quantitatively the position and intensity changes of 110 (green) and 200 (blue)

diffraction, as well as the amorphous peak (magenta), which reflect structure evolution caused by the electron beam.

Fig. 2a-c show the variations of I_{cryst} and $I_{amorphous}$ from PE films with increasing electron dose. At both RT (red symbols) and 98 K (blue symbols) the electron exposure causes a monotonic decrease of I_{cryst}, which is initially very fast and then becomes slower until zero intensity (**Fig.** 2b). Least-square curve fitting on the measured intensity further illustrates that the variations of I_{cryst} are well described by the exponential decay. In contrast, $I_{amorphous}$ at both temperatures exhibits an initial rise followed by a linear intensity drop (**Fig.** 2c). The initial increase of $I_{amorphous}$ coincides with the fast decay of I_{cryst}, reflecting PE amorphization – one of the well-known radiolysis effects caused by the electron beam [1,28]. On the other hand, mass loss from the electron beam irradiation may also contribute to the intensity decrease. To evaluate the crystal radiation sensitivity quantitatively, we define the critical dose as the accumulated dose at which the normalized I_{cryst} drops to $1/e$ (~37%) [1,2,8,24]. It is derived to be ~9.2 e/Å^2 at 98 K but only ~1.1 e/Å^2 at RT (**Table** 1), which are comparable to previous reports (2-6 e/Å^2 at RT and 6.7-8.2 e/Å^2 at cryogenic condition) [10,11,24,25,31,32]. The very low critical dose at RT further evinces the necessity of cryo-protection to achieve reliable structure information from pristine PE samples. Note that the concept of critical dose only describes the dependence of beam effects on the accumulated electron dose without considering the dose rate effect [1,8], which could be a minor effect according to experimental studies in similar polymer films [24,25,35,36].

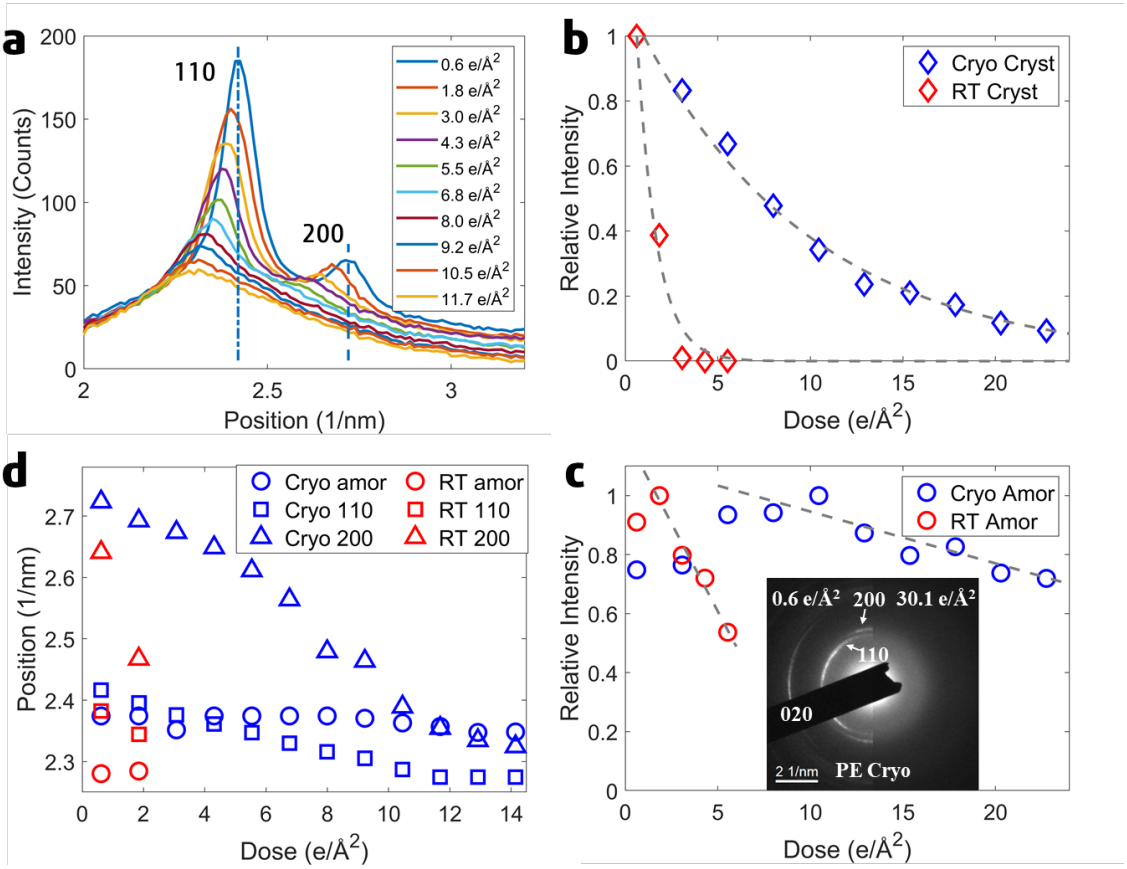

Fig. 2. (a) Radial-averaged intensity profiles of SAED patterns from PE at 98K with different electron doses. Profiles are shifted vertically with an incremental constant in sequence. (b, c) Relative intensity of (b) I_{cryst}, and (c) $I_{amorphous}$ as functions of accumulated electron dose for PE at 98 K (blue) and RT (red), respectively. The exponential and linear decay is indicated by the fitted dashed lines. The intensity is derived from the area of the fitted Gaussians on radial-averaged diffraction peaks, normalized by the maximal intensity of the whole series. Inset in (c) shows SAED patterns on the same PE film at 98 K (cryo) with the dose 0.6 (left) and 30.1 (right) e/Å^2 respectively, illustrating the amorphization process. (d) Peak positions of PE 110 (square), 200 (triangle), and amorphous (circle) diffraction with increasing electron dose, at 98 K (blue) and RT (red), respectively.

The amorphous PE appears to be more stable than the crystalline phase, with $I_{amorphous}$ showing no substantial decreases until I_{cryst} approaching zero. Therefore, diffraction patterns of PE become dominated by the amorphous halo at the late stage of beam exposure, as shown in the inset of **Fig.** 2c. The linear decrease of $I_{amorphous}$ at this stage further indicates that mass loss from beam effects such as bond scission and surface sputtering eventually becomes the prevailing damage process: It has been reported that radiolysis beam effects such as amorphization typically lead to the exponential decay of I_{cryst}, whereas mass loss causes the linear decay [1,8], which rationalizes the different decay behavior between I_{cryst} (exponential) and $I_{amorphous}$ (linear). From the fitted slopes of $I_{amorphous}$, the intensity drop is slowed down by 6.8 times when lowering the temperature from RT to 98 K. It demonstrates that cryo-protection is also effective in prohibiting mass loss in amorphous PE in addition to the above beam effect in the crystalline part.

Table 1. The critical doses of crystalline components in e/Å^2, and their 95% confidence intervals of PE, PCL and P3HT at RT and 98 K derived from the exponential decay of I_{cryst}.

Condition	PE	PCL	P3HT
RT	1.1 (0.5-1.6)	1.9 (1.1-2.7)	7.5 (7.0-8.0)
98 K	9.2 (8.6-9.9)	19.8 (18.2-21.3)	16.3 (14.5-18.0)

Besides intensity variation, we also analyze the change of diffraction peak positions observed in **Fig.** 1a and 2a, which reflects lattice spacing variations upon the beam exposure. As plotted in **Fig.** 2d, the 110 diffraction peak shifts linearly from 2.42 nm^{-1} to 2.29 nm^{-1} at 98 K after accumulating 10.5 e/Å^2 electron dose, corresponding to the increase of lattice spacing d_{110} from 4.13 Å to 4.37 Å, ~5.7% expansion. Meanwhile, the 200 diffraction peak exhibits even more dramatic shifts from 2.72 nm^{-1} to 2.39 nm^{-1}, equivalent

to a ~13.8% expansion from 3.68 Å to 4.18 Å. On the other hand, the amorphous diffraction peak shows negligible shift during the same observation, indicating that the expansion is for the crystal lattice only and thus should not be caused by heating from the electron beam. Indeed, after raising the temperature by 200 K to RT, both 200 and 110 diffraction peaks shift only slightly as shown in **Fig.** 2d (red triangles and squares), which cannot account for the observed large expansion at 98 K and further exclude the effect of beam heating. RT measurement on peak position variations also displays the same trends, only with less data points due to much faster intensity decay.

It is worth noting that the anisotropic lattice expansion has been observed in PE lamellar crystals under electron irradiation, which eventually gives rise to equal d_{110} and d_{200} lattice spacing with a hexagonal SAED pattern, before the complete amorphization [25]. It has been attributed to radiolysis damage and the subsequent crosslinking between polymer chains [25]: with the breaking of chain alignment through bond scission and crosslinking, a lamellar crystal contracts along the chain direction (*c* axis), which leads to the inevitable lateral expansion. Such expansion has been observed explicitly in PE single crystals after irradiation, particularly along the normal of {110} and {200} planes that are the growth surfaces [N2 38]. It is consistent with the larger expansion perpendicular to {200} and {110} planes as shown in Fig. 2d, which coincides with the increase of $I_{amorphous}$ in terms of accumulated dose and thus the amorphization process from radiolysis and crosslinking. On the other hand, the exact mechanism for the anisotropic expansion maximized perpendicular to {200} planes is still unclear, and has been proposed to be caused by the larger intermolecular distance and thus the weaker intermolecular interaction or constraint along the *a* axis [25, N1 35, N3 39].

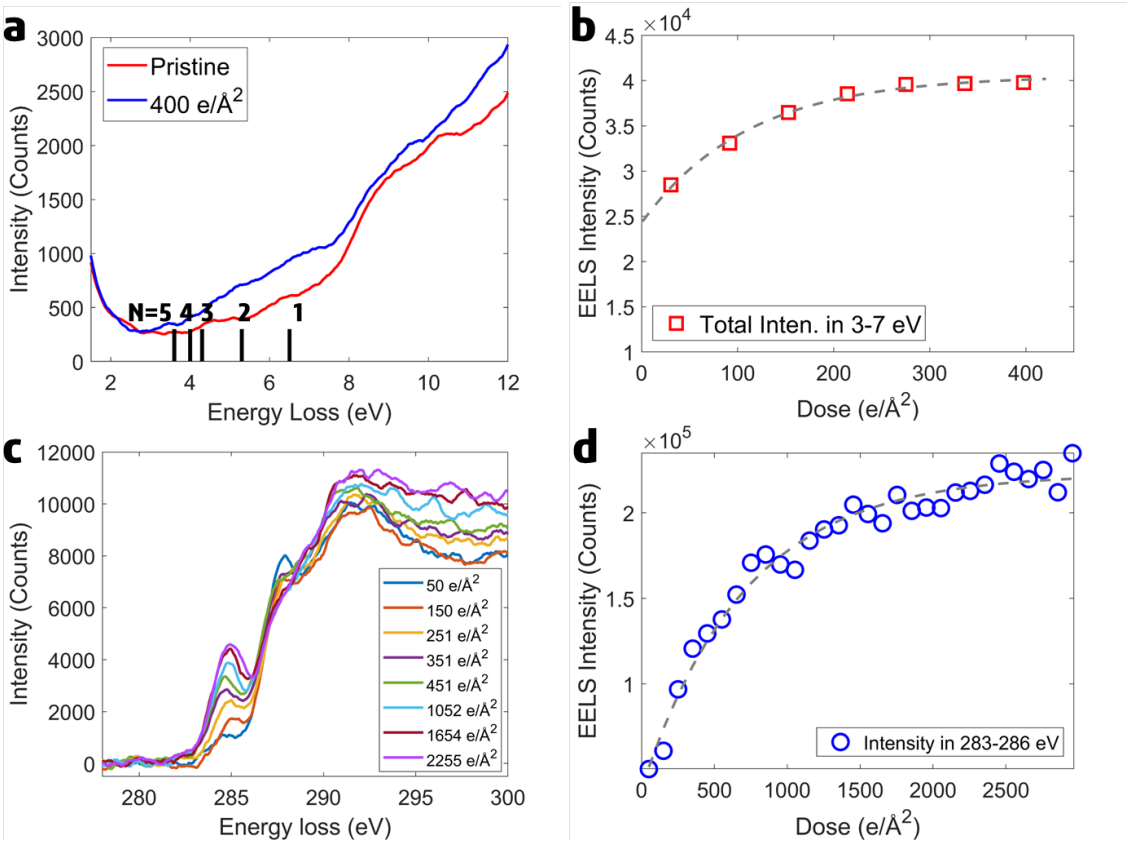

Fig. 3. (a) Comparison of low loss EEL spectra from PE before and after beam exposure at 98 K. The vertical black lines indicate the energy loss associated with polyenyl groups containing *N* unsaturated bonds. (b) Exponential increase of polyenyl groups signal intensity integrated from EELS series in 3-7 eV with increasing electron dose at 98 K. (c) C-K edge EEL spectra of PE under different electron doses. (d) Intensity of C-K edge in the range of 283-286 eV as a function of accumulated electron dose, which follows an exponential increase as shown by the fitted dashed lines. Error bars smaller than the size of marks are not shown.

In addition to the structure analysis based on diffraction, further insights can be obtained by probing the change of chemical bonding using EELS. As shown in **Fig.** 3a, the characteristic energy-loss signal from PE is in the range of 8-11 eV [37], as can be observed

in the pristine PE spectrum (red). With the extended beam exposure, the PE signal becomes flatter (blue spectrum), reflecting the loss of PE material. Interestingly, electron beam exposure also causes an increase of intensity within 3-7 eV, consistent with previous EELS and optical absorption spectrum study of the radiation damage on PE [27,37,38]. This signal is ascribed to the formation of polyenyl groups: C-H bonds are among the most radiation vulnerable bonds [30], possibly owing to its very localized excitation compared to the C-C bonds that can transfer the excitation energy along the polymer chain [N4 42, N5 43]. The easy loss of hydrogen under vacuum may also exaggerate the instability of C-H bonds, making them much more liable to break than the C-C bonds under the radiolysis beam effect. The C-H bond scission gives rise to alkyl radicals (**Fig.** 4a) that can migrate along the single polymer chain via hydrogen hopping [39-41]. When two alkyl radicals meet, they can combine to either form unsaturated bonds along a single chain (**Fig.** 4b) or cause crosslinking between adjacent chains. While crosslinking may be the primary mechanism for amorphization [25, N5], as observed in SAED patterns (Fig. 2), the unsaturated bond formation may continue to generate various polyenyl groups such as dienyl and trienyl chromophores [42], as illustrated in **Fig.** 4b-f. These polyenyl groups have the characteristic energy-loss signal in the range of 3-7 eV [27], as labelled by the number of unsaturated bonds in **Fig.** 3a, which are responsible for the observed signal rise in the beam-exposed PE. The quantitative curve fitting in **Fig.** 3b further depicts that the increase of chromophore signal follow the exponential trend, confirming their origin as the radiolysis beam effect [1,8]. We note that owing to the difficulties modeling the background of low-loss EELS signal, **Fig.** 3b only displays the raw intensity without background subtraction, which contains mixed signals with the contribution from the

plasmon peak and thus unreliable to derive the critical dose from the quantitative fitting in Fig. 3b.

The formation of unsaturated C=C bonds can also be detected using the C-K EELS edge as shown in the **Fig.** 3c. The peak at 285 eV corresponds to 1s-π^* (C=C) transition [27,29,30], which is absent in pristine PE due to no unsaturated C=C bonds. Under electron irradiation, this peak intensity rises exponentially as shown in **Fig.** 3d, evidencing the increasing number of unsaturated bonds, in consistency with low-loss EELS result. The second peak at 287.5 eV that corresponds to 1s-σ^* transition in C-H bonds decreases and broadens, demonstrating that the pristine -CH_2- backbone is damaged by bond scission [29,30]. We have performed EELS measurements in both STEM and TEM modes, which show the similar damage process and critical dose, as demonstrated in **Fig.** S3 in Supplementary Information. It shows that the formation of unsaturated C=C bonds lasts over a much larger dose range compared to SAED measurement and continues at very high dose when PE becomes completely amorphous.

The identified C-H bond scission and subsequently generated polyenyl groups also provide a feasible mechanism for the observed lattice expansion in beam-exposed PE, in addition to the above mentioned crosslinking effect: As illustrated in **Fig.** 4g and 4h, with the formation of unsaturated C=C bonds, the adjacent C-H bonds must rotate (from $H_{1,2}$ to H_5 in **Fig.** 4h for instance) and cause an increased distance (from D_1 to D_2) between the two ending hydrogen atoms H_5 and H_6. Further increasing the number of C=C bonds by radiolysis will create more such protruding hydrogen atoms and effectively cause a swelling of polymer chains, which subsequently pushes the neighboring PE chains apart and leads to the enlarged lattice spacing in PE structure as identified in **Fig.** 2d. Indeed, it

has been reported that the propylene-ethylene copolymers, with propylene units distributed randomly along the linear polyethylene chain, show continuously increasing *a* lattice parameter with an increase of propylene content, while only a slight increase in *b* lattice parameter [N3], consistent with our experimental observation. Moreover, the trans-polybutadiene crystal with one C=C bond in the repeating unit (-CH_2-CH=CH-CH_2-) also has a larger interchain spacing (4.56-4.60 Å) [43,44] compared to pristine PE without C=C bond (~4.4 Å) [45,46], further validating the above proposed mechanism as one possible source of the observed lattice expansion.

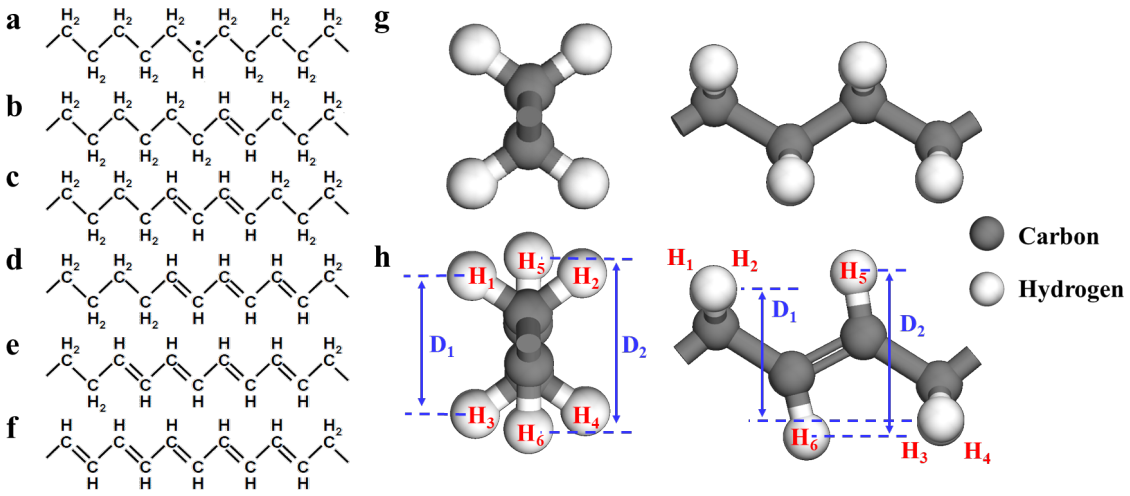

Fig. 4. (a-f) Schematic drawing of the (a) alkyl radical and (b) allyl, (c) dienyl, (d) trienyl, (e) tetraenyl, and (f) pentaenyl groups. (g) Atomic model of the PE repeating unit. (h) Atomic model of a segment of an allyl group to illustrate the effect of C=C bonding on the positions of hydrogen atoms. The six hydrogen atoms are labelled as H_i (i = 1-6) with the projected spacing marked as D_1 and D_2.

Sample	Diffraction	Position (1/nm) at 0.6 e/Å^2	Position (1/nm) at 10.5 e/Å^2	Expansion ratio (%)
PE	200	2.72	2.39	13.8
	020	4.02	3.92	2.6
	110	2.42	2.29	6.1
		at 0.9 e/Å^2	at 10.1 e/Å^2	
PCL	200	2.71	2.58	5.0
	020	3.97	3.95	0.5
	110	2.41	2.37	1.7

Table 2. Peak positions of 200, 020 (detailed data shown in Supplementary **Fig.** S4) and 110 diffraction and the corresponding expansion ratio for PE and PCL after beam exposure at 98 K. Errors of positions are all below than 0.01 1/nm.

Fig. 5 presents the detected beam effects on PCL spherulite thin films, which are remarkably close to that observed in PE . Owing to the similar crystal structure to PE, SAED of PCL is also dominated by 110 and 200 diffraction (**Fig.** 5a and the inset of **Fig.** 5c). With accumulating more electron dose, both diffraction signals become weaker and shift towards the central beam. Curve modelling on the radial-averaged SAED profiles illustrates these trends quantitatively: as displayed in **Fig.** 5b and 5c for both temperatures the decay of PCL I_{cryst} is exponential with a faster initial drop that matches the increase of $I_{amorphous}$ at the early stage (**Fig.** 5c), a sign of amorphization owing to the radiolysis damage. This is further evidenced by the amorphous halo that dominates the diffraction

pattern at the final stage of beam exposure (inset of **Fig.** 5c). The amorphization becomes considerably slower at 98 K, proving again the effectiveness of cryo-protection. On the other hand, the linear decrease of $I_{amorphous}$ at the late stage still demonstrates mass loss as the dominating beam effect when I_{cryst} approaches zero. At both temperatures, beam effects on PCL appear to be slower than on PE, as reflected by the higher critical doses derived for PCL (**Table** 1).

Fig. 5d shows the shift of 110 and 200 PCL diffraction, reflecting lattice expansion similar to PE. The shift is more rapid at RT and is larger for 200 diffraction (see **Table 2**), suggesting the similar anisotropic expansion. The amorphous diffraction peak still shows negligible shift, excluding the heating effect as the cause of lattice expansion. EELS on the exposed PCL (**Fig.** 6a and 6c) also exhibits the exponentially enhanced signals in both low-loss (3-7 eV) and C-K edge (283-286 eV) EEL spectra (**Fig.** 6b and 6d), corresponding to the formation of polyenyl groups and unsaturated C=C bonds from the radiolysis beam effect, which is presumably responsible for the observed amorphization and lattice expansion similar to PE films. All these observations are in notable agreement with results from PE films, suggesting the same damage mechanism in both materials, probably owing to their similar crystal structure, polymer backbone structure, as well as sample thicknesses.

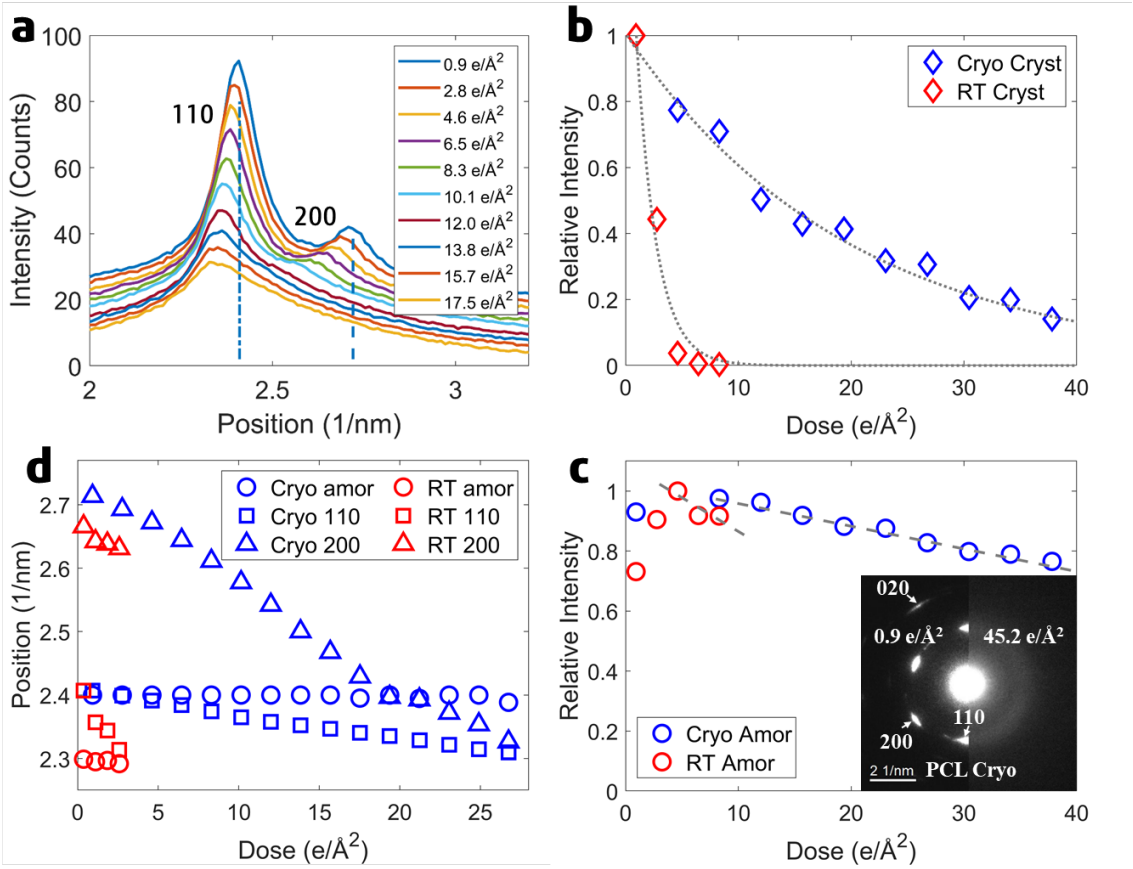

Fig. 5. (a) Radial-averaged intensity profiles of SAED patterns from PCL at 98K under different electron doses. Profiles are shifted vertically with an incremental constant in sequence. (b, c) Relative intensity of (b) I_{cryst}, and (c) $I_{amorphous}$ as functions of accumulated electron dose for PCL at 98 K (blue) and RT (red), respectively. The exponential and linear decay is indicated by the fitted dashed lines. Inset in (c) shows SAED patterns on the same PCL film at 98 K (cryo) with the dose 0.9 (left) and 45.2 (right) e/Å^2 respectively, illustrating the amorphization process. (d) Peak positions of PCL 110 (square), 200 (triangle), and amorphous (circle) diffraction with increasing electron dose, at 98 K (blue) and RT (red), respectively.

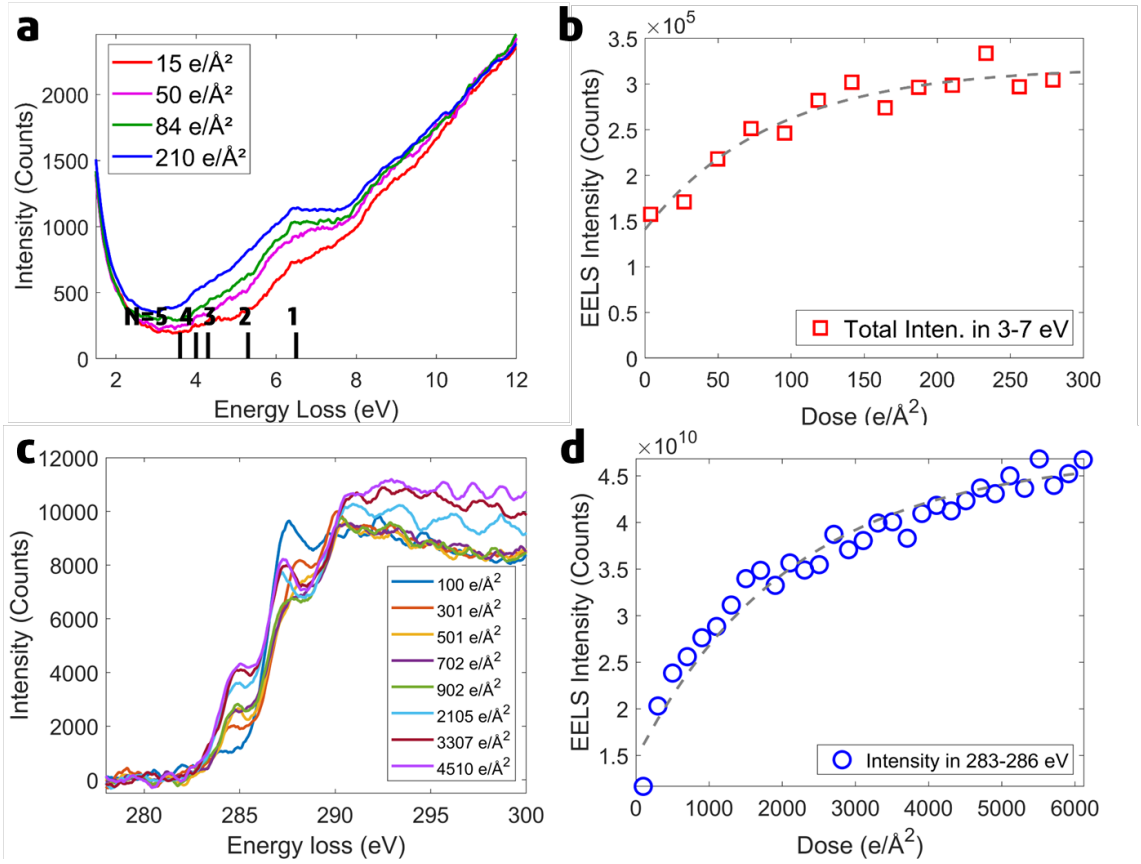

Fig. 6. (a) Comparison of low loss EEL spectra from PCL under various electron doses at 98 K. The vertical black lines indicate the energy loss associated with polyenyl groups containing *N* unsaturated bonds. (b) Increase of polyenyl group signal (3-7 eV measured from EELS series in (a)) with increasing electron dose on PCL at 98 K, which follows an exponential function. (c) C-K edge EEL spectra of PCL under different electron doses. (d) Intensity of C-K edge in the range of 283-286 eV in (c) as a function of accumulated electron dose, which follows an exponential increase as shown by the fitted dashed lines. Error bars smaller than the size of marks are not shown.

In contrast, P3HT spherulite thin films with the conjugated π bonding show distinct degradation behavior as compared to PE and PCL, demonstrating complexity of beam effects in organic solids. The CS_2 vapor annealing (see Materials and Methods) makes

P3HT crystallize in the *Form-II* structure [51-53] (a = 13.5 Å, b = 9.1 Å, c = 7.9 Å, γ=69.3°) with the (320) normal along the π-stacking direction and c axis along the backbone direction, consistent with previous reports in literature [54-56]. The mobility measurement further indicates that the backbone direction and the π-stacking direction should be primarily in plane [57-59], which is in accordance with the strong 002_{II} and 320_{II} diffraction signals observed at 98 K (2.57 and 2.67 nm^{-1} as shown in **Fig.** 7a and 7c). Interestingly, after accumulating 20.3 e/Å^2 electron dose, 002_{II} becomes much dimmer compared to 320_{II} diffraction. The radial-averaged SAED profiles in **Fig.** 7c further demonstrate the quick decay of 002_{II} diffraction at the early stage of beam exposure, with 320_{II} diffraction peak remaining relatively stable, as also revealed quantitatively by the associated diffraction intensity derived from Gaussian modeling shown in **Fig.** 7e. Only after the extinction of 002_{II} diffraction, the decay of 320_{II} diffraction starts with an intensity plateau separating the exponential decay of the two diffraction signals. Since 002_{II} diffraction reflects the ordering of the side chains while 320_{II} represents the π-stacking ordering, the above two-stage decay process indicates that the electron beam preferentially alters the side chains first, while the π-conjugated polythiophene backbones are more robust to electron irradiation. We note that such a two-stage beam effect in P3HT has never been reported before.

RT measurements on P3HT do not show the two-stage decay due to the absence of 002_{II} diffraction even in the first SAED pattern (**Fig.** 7b and 7d). It may be due to the order-to-disorder transition for the side chains that has been reported in P3HT around RT[ACS Mater. Inter.], while we cannot rule out the possibility of beam damage to destroy the susceptible side-chain ordering with the electron dose as low as 0.6 e/Å^2. Further beam exposure at RT

leads to diffused diffraction halos reflecting the amorphization process. This restricts us to using the decay of 320_{II} diffraction to derive the critical dose of P3HT at RT, while the critical dose at 98 K is derived from the decay of 002_{II} diffraction, both values are presented in **Table** 1. The higher critical dose for P3HT can be attributed to the presence of the conjugated π-electron system and the lack of C-H bonds on its backbone compared to PE and PCL [8,28], which also explains the damage of the side chains (consisting of C-H bonds) prior to the π-conjugated backbones. On the other hand, our P3HT critical dose is considerably lower than previous reports [10,24], which may be due to the smaller film thickness (~15 nm vs. ~90 nm [10]) as well as the potentially different polymorphs (*Form-II* vs. *Form-I*).

Besides revealing the two-stage damage process, **Fig.** 7e also demonstrates the suppression of radiolysis effect in P3HT spherulite thin films at cryogenic temperature: When I_{cryst} approaches zero at ~50 e/Å^2 dose (**Fig.** 7e), $I_{amorphous}$ also becomes negligible at 98 K (**Fig.** 7f), in contrast to the considerable $I_{amorphous}$ at RT when I_{cryst} drops to zero. As a result, there is no amorphous diffraction halo forming in P3HT at 98 K, indicating the suppressed amorphization process. Moreover, at 98 K shown in **Fig.** 7f, $I_{amorphous}$ decreases monotonically without any increasing stage, in contrast to the initially rising $I_{amorphous}$ at RT (red circles) as well as for PE and PCL films (**Fig.** 2c and 5c). It implies that mass loss due to knock-on effect dominates from the beginning of beam exposure, presumably due to the suppression of radiolysis at cryogenic temperature. The peak position analysis shown in **Fig.** 7g also illustrates that only at RT we can see the shift of 320_{II} diffraction from 2.67 to 2.55 nm^{-1} after accumulating 16.0 e/Å^2 dose, while no shift can be consistently detected at 98 K. As lattice expansion is attributed to the radiolysis beam effect, it further evidences

the suppressed radiolysis in P3HT at cryogenic condition. The inelastic mean free path of electrons is about 100-200 nm in common polymers at RT [60,61] and increases further with decreasing temperature [62]. Thus at 98 K the inelastic mean free path should be substantially larger than the thickness of P3HT films (~15 nm), explaining the suppressed inelastic scattering and the radiolysis effect. On the other hand, the effect of cryo-protection on mass loss appears to be limited in P3HT, as reflected by the similar decay rates at the two temperatures for both I_{cryst} and $I_{amorphous}$ (**Fig.** 7e and 7f).

The characteristic EELS signal corresponding to the interband transitions in P3HT at 98 K is presented in **Fig.** 7h, where the edge onset from the pristine sample (after accumulating 4 e/Å^2 dose) matches its bandgap energy ~1.7 eV [28,63]. With increasing electron dose, the signal intensity in range of 1.5 to 3.5 eV decreases linearly (**Fig.** 7i), which is characteristic of mass loss [1,8] and also consistent with the suppression of the radiolysis effect at this low temperature. Moreover, a shift of the EELS edge onset towards higher energies, from 1.73 to 2.14 eV after accumulating 119 e/Å^2 dose, is also observed (**Fig.** 7h and 7i). Both the intensity drop and energy shift are in accordance with the previous EELS study on P3HT [28]. In addition, the signal in the range of 3-7 eV remains constant throughout the whole process of beam exposure, indicating the absence of polyenyl group formation and therefore a very different damage mechanism from PE and PCL films.

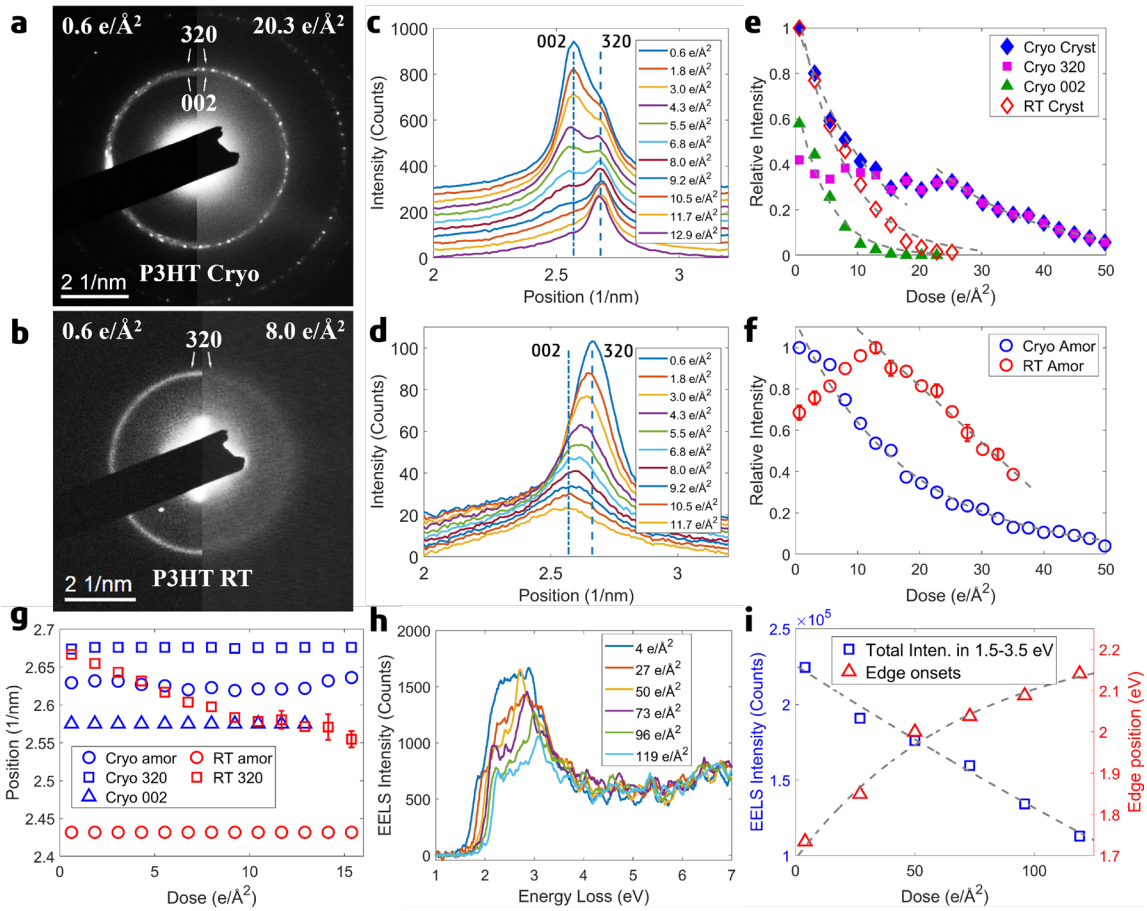

Fig. 7. (a-d) SAED patterns and the corresponding radial-averaged intensity profiles from P3HT films under different electron doses at (a,c) 98 K and (b,d) RT, respectively. Profiles are shifted vertically with an incremental constant in sequence. (e) I_{cryst} and (f) $I_{amorphous}$ as functions of accumulated electron dose for P3HT at 98 K (blue) and RT (red), respectively. The exponential and linear decay is indicated by the fitted dashed lines. (g) Peak positions of 320_{II} (square) and amorphous (circle) diffraction under the increasing electron dose at 98 K (blue) and RT (red), respectively, and peak position of 002_{II} diffraction (blue triangle) at 98 K. (h) Comparison of background-subtracted EEL spectra under different electron doses at 98 K. (i) Change of P3HT integrated EELS intensity in the range of 1.5 to 3.5 eV (blue square), and shift of the EELS edge onset (red triangle) with increasing electron dose

at 98 K. The exponential and linear decay is indicated by the fitted dashed lines. Error bars smaller than the size of marks are not shown.

CONCLUSIONS

In summary, we have characterized the effects of high-energy electron beam on PE, PCL, and P3HT spherulite thin films at room and cryogenic temperatures, through analyzing quantitatively both SAED and EELS under different electron doses. By distinguishing signals from crystalline and amorphous phases, beam effects including mass loss and amorphization have been clearly identified, most of which can be suppressed effectively by cryo-protection. For PE and PCL, beam effects are initially dominated by radiolysis, which leads to amorphization as well as lattice expansion. EELS analysis further unravels the formation of unsaturated polyenyl groups generated by radiolysis of C-H bonds, providing a feasible mechanism for both amorphization and lattice expansion processes. At the late stage, both PE and PCL appear to be largely amorphized, with the linear decrease of the amorphous phase owing to mass loss. On the other hand, P3HT exhibits a more complicated two-stage damage process at cryogenic temperature, with the side-chain ordering preferentially damaged before the π-stacking ordering. The suppressed radiolysis effect in P3HT at cryogenic temperature is also identified, which can be attributed to both cryo-protection and ultrathin film thickness compared to the inelastic mean free path. At last, the unraveled damage mechanisms in this work have demonstrated the power of our quantitative analysis on understanding the detailed beam effects on structure and chemical bonding of organic solids, which should offer valuable guidance for optimizing TEM imaging conditions under the controlled electron dose, to achieve pristine sample information with minimized artefacts.

ACKNOWLEDGMENT

This work was supported by the Research Grants Council of Hong Kong (No. 15304919 and C5029-18E) and the Hong Kong Polytechnic University grant (No. ZVRP). The authors thank Dr. Wei Lu for optimizing the electron microscopes, and Min Chen for providing polymer samples as well as helpful discussion.

REFERENCE

(1) Egerton, R. F., Radiation damage to organic and inorganic specimens in the TEM. Micron *119* (2019) 72-87.

(2) Egerton, R. F., Li, P., Malac, M., Radiation damage in the TEM and SEM. Micron 35 (2004) 399-409.

(3) Carter, C. B., Williams, D. B., Transmission electron microscopy: Diffraction, imaging, and spectrometry. Springer: 2016.

(4) Sawyer, L., Grubb, D. T., Meyers, G. F., Polymer microscopy. Springer Science & Business Media: 2008.

(5) Karuppasamy, M., Karimi Nejadasl, F., Vulovic, M., Koster, A. J., Ravelli, R. B., Radiation damage in single-particle cryo-electron microscopy: effects of dose and dose rate. J. Synchrotron Radiat. 18 (2011) 398-412.

(6) Ueno, T., Nakashima, E., & Takeda, K. (2010). Quantitative analysis of random scission and chain-end scission in the thermal degradation of polyethylene. Polym. Degrad. Stab. 95 (2010) 1862-1869.

(7) Uchida, K., Shimizu, N., The effect of temperature and voltage on polymer chain scission in high-field region. IEEE Trans. Dielectr. Electr. Insul. 26 (1991) 271-277.

(8) Chen, Q., Dwyer, C., Sheng, G., Zhu, C., Li, X., Zheng, C., Zhu, Y., Imaging Beam-Sensitive Materials by Electron Microscopy. Adv. Mater. 32 (2020) 1907619.

(9) Duyvesteyn, H. M. E., Kotecha, A., Ginn, H. M., Hecksel, C. W., Beale, E. V., de Haas, F., Evans, G., Zhang, P., Chiu, W., Stuart, D. I., Machining protein microcrystals for structure determination by electron diffraction. Proc. Natl. Acad. Sci. U S A 115 (2018) 9569-9573.

(10) Kuei, B., Bator, C., Gomez, E. D., Imaging 0.36 nm Lattice Planes in Conjugated Polymers by Minimizing Beam Damage. Macromolecules 53 (2020) 8296-8302.

(11) Kuei, B., Gomez, E. D., Pushing the limits of high-resolution polymer microscopy using antioxidants. Nat. Commun. 12 (2021) 153.

(12) Henson, Z. B., Mullen, K., Bazan, G. C., Design strategies for organic semiconductors beyond the molecular formula. Nat. Chem. 4 (2012) 699-704.

(13) Willhammar, T., Daicho, K., Johnstone, D. N., Kobayashi, K., Liu, Y., Midgley, P. A., Bergstrom, L., Saito, T., Local Crystallinity in Twisted Cellulose Nanofibers. ACS Nano 15 (2021) 2730-2737.

(14) Yang, Y., Chen, H., Li, H., Polymer single crystal dielectrics for organic field-effect transistors. Polymer 137 (2018) 255-260.

(15) Panova, O., Ophus, C., Takacs, C. J., Bustillo, K. C., Balhorn, L., Salleo, A., Balsara, N., Minor, A. M., Diffraction imaging of nanocrystalline structures in organic semiconductor molecular thin films. Nat. mater. 18 (2019) 860-865.

(16) Xu, H., Lebrette, H., Clabbers, M. T., Zhao, J., Griese, J. J., Zou, X., Högbom, M., Solving a new R2lox protein structure by microcrystal electron diffraction. Sci. Adv. 5 (2019) eaax4621.

(17) Clabbers, M. T. B., van Genderen, E., Wan, W., Wiegers, E. L., Gruene, T., Abrahams, J. P., Protein structure determination by electron diffraction using a single three-dimensional nanocrystal. Acta Crystallogr. D 73 (2017) 738-748.

(18) Cui, P., Svensson Grape, E., Spackman, P. R., Wu, Y., Clowes, R., Day, G. M., Inge, A. K., Little, M. A., Cooper, A. I., An expandable hydrogen-bonded organic framework characterized by three-dimensional electron diffraction. J. Am. Chem. Soc. 142 (2020) 12743-12750.

(19) Navas, J., Sánchez-Coronilla, A., Gallardo, J. J., Piñero, J. C., De los Santos, D., Martín, E. I., Hernández, N. C., Alcántara, R., Fernández-Lorenzo, C., Martín-Calleja, J., The impact of Pd on the light harvesting in hybrid organic-inorganic perovskite for solar cells. Nano Energy 34 (2017) 141-154.

(20) Yamaguchi, A., Nemoto, T., Kurata, H., Study of C K-Edge High Energy Resolution Energy-Loss Near-Edge Structures of Copper Phthalocyanine and Its Chlorinated Molecular Crystals by First-Principles Band Structure Calculations. J. Phys. Chem. A. 124 (2020) 1735-1743.

(21) Stoeckel, M. A., Olivier, Y., Gobbi, M., Dudenko, D., Lemaur, V., Zbiri, M., Guilbert, A. A. Y., D'Avino, G., Liscio, F., Migliori, A., Ortolani, L., Demitri, N., Jin, X., Jeong, Y. G., Liscio, A., Nardi, M. V., Pasquali, L., Razzari, L., Beljonne, D., Samori, P., Orgiu, E., Analysis of External and Internal Disorder to Understand Band-Like Transport in n-Type Organic Semiconductors. Adv. Mater. 33 (2021) 2007870.

(22) Pedrosa, M., Drazic, G., Tavares, P. B., Figueiredo, J. L., Silva, A. M. T., Metal-free graphene-based catalytic membrane for degradation of organic contaminants by persulfate activation. Chem. Eng. J. 369 (2019) 223-232.

(23) Duan, X., Ao, Z., Zhang, H., Saunders, M., Sun, H., Shao, Z., Wang, S., Nanodiamonds in sp 2 /sp 3 configuration for radical to nonradical oxidation: Core-shell layer dependence. Appl. Catal. B: Environ. 222 (2018) 176-181.

(24) Leijten, Z., Keizer, A. D. A., de With, G., Friedrich, H., Quantitative Analysis of Electron Beam Damage in Organic Thin Films. J. Phys. Chem. C 121 (2017) 10552-10561.

(25) Kobayashi, K., Sakaoku, K., The Changes of Polymer Crystals due to Irradiation with Electrons Accelerated at Various Voltages (Special Issue on Electron Microscopy). Bull. inst. chem. res., Kyoto univ. 42 (1965) 473-493.

(26) Hayward, S. B., Glaeser, R. M., Radiation damage of purple membrane at low temperature. Ultramicroscopy 4 (1979) 201-210.

(27) Ritsko, J. J., Electron energy loss spectroscopy of pristine and radiation damaged polyethylene. J. Chem. Phys. 70 (1979) 5343-5349.

(28) Guo, C., Allen, F. I., Lee, Y., Le, T. P., Song, C., Ciston, J., Minor, A. M., Gomez, E. D., Probing Local Electronic Transitions in Organic Semiconductors through Energy-Loss Spectrum Imaging in the Transmission Electron Microscope. Adv. Funct. Mater. 25 (2015) 6071-6076.

(29) Leijten, Z. J., Wirix, M. J., Lazar, S., Verhoeven, W., Luiten, O. J., de With, G., Friedrich, H., Nanoscale chemical analysis of beam-sensitive polymeric materials by cryogenic electron microscopy. J. Polym. Sci 59 (2021) 1221-1231.

(30) Varlot, K., J. M. Martin, C. Quet, EELS analysis of PMMA at high spatial resolution. Micron 32 (2001) 371-378.

(31) Egerton, R., Rauf, I., Dose-rate dependence of electron-induced mass loss from organic specimens. Ultramicroscopy 80 (1999) 247-254.

(32) Drummy, L. F., Yang, J., Martin, D. C., Low-voltage electron microscopy of polymer and organic molecular thin films. Ultramicroscopy 99 (2004) 247-56.

(33) Kisielowski, C., Specht, P., Freitag, B., Kieft, E. R., Verhoeven, W., van Rens, J. F., Yancey, D. F., Discovering hidden material properties of MgCl2 at atomic resolution with structured temporal electron illumination of picosecond time resolution. Adv. Funct. Mater 29 (2019) 1807818.

(34) VandenBussche, Elisah J., David J. Flannigan, Reducing radiation damage in soft matter with femtosecond-timed single-electron packets. Nano letters 19 (2019) 6687-6694.

(35) Egerton, R. F., Lazar, S., Libera, M., Delocalized radiation damage in polymers. Micron 43 (2012) 2-7.

(36) Egerton, R., Crozier, P., Rice, P., Electron energy-loss spectroscopy and chemical change. Ultramicroscopy 23 (1987) 305-312.

(37) Bodily, D. M., Dole, M., Ultraviolet Spectroscopy of Irradiated Polyethylene. J. Chem. Phys. 45 (1966) 1428-1432.

(38) Jones Jr, L., Taylor, L., Far ultraviolet absorption spectra of unsaturated and aromatic hydrocarbons. Anal. Chem. 27 (1955) 228-237.

(39) Singh, A., Irradiation of polyethylene: Some aspects of crosslinking and oxidative degradation. Radiat. Phys. Chem. 56 (1999) 375-380.

(40) Dole, M., Cracco, F., Radiation chemistry of polyethylene. V. Hydrogen isotope exchange studies. J. Phys. Chem. 66 (1962) 193-201.

(41) Clough, R. L., Isotopic exchange in gamma-irradiated mixtures of C24H50 and C24D50: Evidence of free radical migration in the solid state. J. Chem. Phys. 87 (1987) 1588-1595.

(42) Waterman, D., Dole, M., Radiation chemistry of polyethylene. X. Kinetics of the conversion of alkyl to allyl free radicals. J. Phys. Chem. 74 (1970) 1913-1922.

(43) Suehiro, K., Takayanagi, M., Structural studies of the high temperature form of trans-1, 4-polybutadiene crystal. J. Macromol. Sci. B 4 (1970) 39-46.

(44) Iwayanagi, S., Sakurai, I., Sakurai, T., Seto, T., X-ray structure analysis of trans-1, 4-polybutadiene. J. Macromol. Sci. B 2 (1968) 163-177.

(45) Kleis, J., Lundqvist, B. I., Langreth, D. C., Schröder, E., Towards a Working Density-Functional Theory for Polymers: First-Principles Determination of the Polyethylene Crystal Structure. Phys. Rev. B 76 (2007) 100201.

(46) Teare, P. W., The crystal structure of orthorhombic hexatriacontane, C36H74. Acta Crystallogr. 12.4 (1959) 294-300.

(47) Toda, A., Okamura, M., Hikosaka, M., Nakagawa, Y. Three-dimensional shape of polyethylene single crystals grown from dilute solutions and from the melt. Polymer 46 (2005) 8708-8716.

(48) Hu, Wenbing, The physics of polymer chain-folding. Phys. Rep 747 (2018) 1-50.

(49) Wittmann, J. C., and B. Lotz. Polymer decoration: the orientation of polymer folds as revealed by the crystallization of polymer vapors. J. Polym. Sci. Polym. Phys. Ed. 23 (1985) 205-226.

(50) Weber, C. H., Chiche, A., Krausch, G., Rosenfeldt, S., Ballauff, M., Harnau, L., Single lamella nanoparticles of polyethylene. Nano Letters 7 (2007) 2024-2029.

(51) Brinkmann, M., Structure and morphology control in thin films of regioregular poly (3‐hexylthiophene). J. Polym. Sci. B: Polym. Phys. 49 (2011) 1218-1233.

(52) Lu, G., Li, L., Yang, X., Achieving Perpendicular Alignment of Rigid Polythiophene Backbones to the Substrate by Using Solvent‐Vapor Treatment. Adv. Mater. 19 (2007) 3594-3598.

(53) Lu, G., Li, L., Yang, X., Morphology and crystalline transition of poly(3-butylthiophene) associated with its polymorphic modifications. Macromolecules 41 (2008) 2062-2070.

(54) Rahimi, K., Botiz, I., Stingelin, N., Kayunkid, N., Sommer, M., Koch, F. P. V., Nguyen, H., Coulembier, O., Dubois, P., Brinkmann, M., Controllable processes for generating large single crystals of poly(3‐hexylthiophene). Angew. Chem. Int. Ed. 51 (2012) 11131-11135.

(55) Zhugayevych, A., Mazaleva, O., Naumov, A., Tretiak, S., Lowest-energy crystalline polymorphs of P3HT. J. Phys. Chem. C 122 (2018) 9141-9151.

(56) Koch, F. P. V., Heeney, M., Smith, P., Thermal and structural characteristics of oligo(3-hexylthiophene)s(3HT) n, n= 4–36. J. Am. Chem. Soc. 135 (2013) 13699-13709.

(57) Crossland, E. J., Tremel, K., Fischer, F., Rahimi, K., Reiter, G., Steiner, U., Ludwigs, S., Anisotropic Charge Transport in Spherulitic Poly (3‐hexylthiophene) Films. Adv. Mater., 24 (2012) 839-844.

(58) Sirringhaus, H., Brown, P., Friend, R., Nielsen, M. M., Bechgaard, K., Langeveld-Voss, B., Spiering, A., Janssen, R. A., Meijer, E., Herwig, P., Two-dimensional charge transport in self-organized, high-mobility conjugated polymers. Nature 401 (1999) 685-688.

(59) Kline, R. J., McGehee, M. D., Kadnikova, E. N., Liu, J., Fréchet, J. M., Toney, M. F., Dependence of regioregular poly (3-hexylthiophene) film morphology and field-effect mobility on molecular weight. Macromolecules 38 (2005) 3312-3319.

(60) Cumpson, P. J., Estimation of inelastic mean free paths for polymers and other organic materials: use of quantitative structure–property relationships. Surf. Interface. Anal. 31 (2001) 23-34.

(61) Iakoubovskii, K., Mitsuishi, K., Nakayama, Y., Furuya, K., Mean free path of inelastic electron scattering in elemental solids and oxides using transmission electron microscopy: Atomic number dependent oscillatory behavior. Phys. Rev. B 77 (2008) 104102.

(62) Li, Q., Das Sarma, S., Finite temperature inelastic mean free path and quasiparticle lifetime in graphene. Phys. Rev. B 87 (2013) 085406.

(63) Al-Ibrahim, M., Roth, H.-K., Schroedner, M., Konkin, A., Zhokhavets, U., Gobsch, G., Scharff, P., Sensfuss, S., The influence of the optoelectronic properties of poly (3-alkylthiophenes) on the device parameters in flexible polymer solar cells. Org. Electron. 6 (2005) 65-77.

New ref

(35) Kakudo, M., Ullman, R., Polyethylene crystallinity from x-ray studies. J. Polym. Sci 1960, 45 (145), 91-104.

(38) Grubb, D. T., Keller, A., Origin of contrast effects in the electron microscopy of polymers. J. Mater. Sci. 1972, 7 (7), 822-835.

(39) Swan, P. R., Polyethylene unit cell variations with temperature. J. Polym. Sci 1962, 56 (164), 403-407.

(42) Partridge, R. H., Excitation Energy Transfer in Alkanes. I. Exciton Model. J. Chem. Phys. 1970, 52 (5), 2485-2490.

(43) Grubb, D. T., Review Radiation-Damage and Electron-Microscopy of Organic Polymers. J. Mater. Sci. 1974, 9 (10), 1715-1736.